sustainability

MDPI

Article

Performance Evaluation of a Prestressed Belitic Calcium Sulfoaluminate Cement (BCSA) Concrete Bridge Girder

Nick Markosian [1], Raed Tawadrous [2], Mohammad Mastali [3], Robert J. Thomas [4] and Marc Maguire [3,*]

1 Calder Richards Structural Consulting Engineers, Salt Lake City, UT 84101, USA; nick@crceng.com
2 eConstruct, Orlando, FL 32817, USA; raed.tawadrous@gmail.com
3 Durham School of Architectural Engineering and Construction, University of Nebraska-Lincoln, Omaha, NE 68182, USA; mmastali2@unl.edu
4 Department of Civil Engineering, Clarkson University, Potsdam, NY 13699, USA; rthomas@clarkson.edu
* Correspondence: marc.maguire@unl.edu

Abstract: Belitic calcium sulfoaluminate (BCSA) cement is a sustainable alternative to Portland cement that offers rapid setting characteristics that could accelerate throughput in precast concrete operations. BCSA cements have lower carbon footprint, embodied energy, and natural resource consumption than Portland cement. However, these benefits are not often utilized in structural members due to lack of specifications and perceived logistical challenges. This paper evaluates the performance of a full-scale precast, prestressed voided deck slab bridge girder made with BCSA cement concrete. The rapid-set properties of BCSA cement allowed the initial concrete compressive strength to reach the required 4300 psi release strength at 6.5 h after casting. Prestress losses were monitored long-term using vibrating wire strain gages cast into the concrete at the level of the prestressing strands and the data were compared to the American Association of State Highway and Transportation Officials Load and Resistance Factor Design (AASHTO LRFD) predicted prestress losses. AASHTO methods for prestress loss calculation were overestimated compared to the vibrating wire strain gage data. Material testing was performed to quantify material properties including compressive strength, tensile strength, static and dynamic elastic modulus, creep, and drying and autogenous shrinkage. The material testing results were compared to AASHTO predictions for creep and shrinkage losses. The bridge girder was tested at mid-span and at a distance of 1.25 times the depth of the beam (1.25*d*) from the face of the support until failure. Mid-span testing consisted of a crack reopening test to solve for the effective prestress in the girder and a flexural test until failure. The crack reopen effective prestress was compared to the AASHTO prediction and AASHTO appeared to be effective in predicting losses based on the crack reopen data. The mid-span failure was a shear failure, well predicted by AASHTO LRFD. The 1.25*d* test resulted in a bond failure, but nearly developed based on a moment curvature estimate indicating the AASHTO bond model was conservative.

Keywords: prestressed concrete; prestress losses; bridges; flexural strength; shear strength; drying and autogenous shrinkage; creep; sustainability

check for updates

Citation: Markosian, N.; Tawadrous, R.; Mastali, M.; Thomas, R.J.; Maguire, M. Performance Evaluation of a Prestressed Belitic Calcium Sulfoaluminate Cement (BCSA) Concrete Bridge Girder. *Sustainability* **2021**, *13*, 7875. https://doi.org/10.3390/su13147875

Academic Editor: Jorge de Brito

Received: 21 May 2021
Accepted: 11 July 2021
Published: 14 July 2021

Publisher's Note: MDPI stays neutral with regard to jurisdictional claims in published maps and institutional affiliations.

Copyright: © 2021 by the authors. Licensee MDPI, Basel, Switzerland. This article is an open access article distributed under the terms and conditions of the Creative Commons Attribution (CC BY) license (https://creativecommons.org/licenses/by/4.0/).

1. Introduction

Calcium sulfoaluminate (CSA) cements are a class of hydraulic cements based on Ye'elimite ($C_4A_3\overline{S}$) which were first patented by Klein in 1964 and 1966 [1,2]. Depending on the specific chemistry and blend, CSA cements can be shrinkage-compensating, rapid-setting, or both. CSA cements include accelerating additives, shrinkage-compensating additives, and standalone cements. Type K shrinkage-compensating cements, for example, rely on up to 5% Ye'elimite for their expansive characteristics. Standalone CSA cements, which are used as single cements rather than blended with Portland cement, have been developed in both the United States and China. In China, "high-CSA" cements that contain Ye'elimite as the predominate phase have been used for many years.

In the United States, Ost et al. [3] introduced standalone belitic calcium sulfoaluminate (BCSA) cements in the 1970s. BCSA cements are rapid setting cements comprising 20–30% Ye'elemite and 30–60% belite interground with 5–25% calcium sulfate, by mass. Rapid early strength development is the hallmark property of BCSA cement, but it is also increasingly viewed as a potential sustainable alternative to Portland cement [4]. The embodied energy and carbon dioxide emissions are significantly lower than Portland cement, owing to several factors including:

1. Lower clinkering temperature, which reduces the energy and emissions associated with firing the kiln [5];
2. Less calcium oxide in the clinker, which reduces the release of CO_2 associated with calcination;
3. Increased friability, which reduces the energy consumption of grinding [6]; and
4. Higher proportion of interground components (e.g., calcium sulfate) that do not require firing, further reducing the embodied energy and emissions associated with clinkering.

Further, a variety of industrial and municipal wastes can be used as precursors, reducing the environmental impact of mining and quarrying raw materials for cement production [7,8].

Figure 1 shows a comparison of the embodied CO_2 emissions for the component phases of Portland and BCSA cements, based on an analysis by Gartner [9]. Accordingly, alite and belite are the main responsible phases for releasing CO_2 into the atmosphere. Generally, Portland cement comprises different cement phases, including 63% alite, 15% belite, 8% tricalcium aluminate, 9% ferrite, 5% others; in comparison, BCSA cement ingredients by 22–71% belite (depends on the sulfate content), 3–7% ferrite, 65–15% calcium sulfoaluminate cement (Ye'elimite). Considering CO_2 emission and the content of each phase of Portland and BCSA cement, Gartner and Sui concluded that BCSA cement could have up to 30% lower CO_2 emission than Portland cement, depending on the phase composition [10].

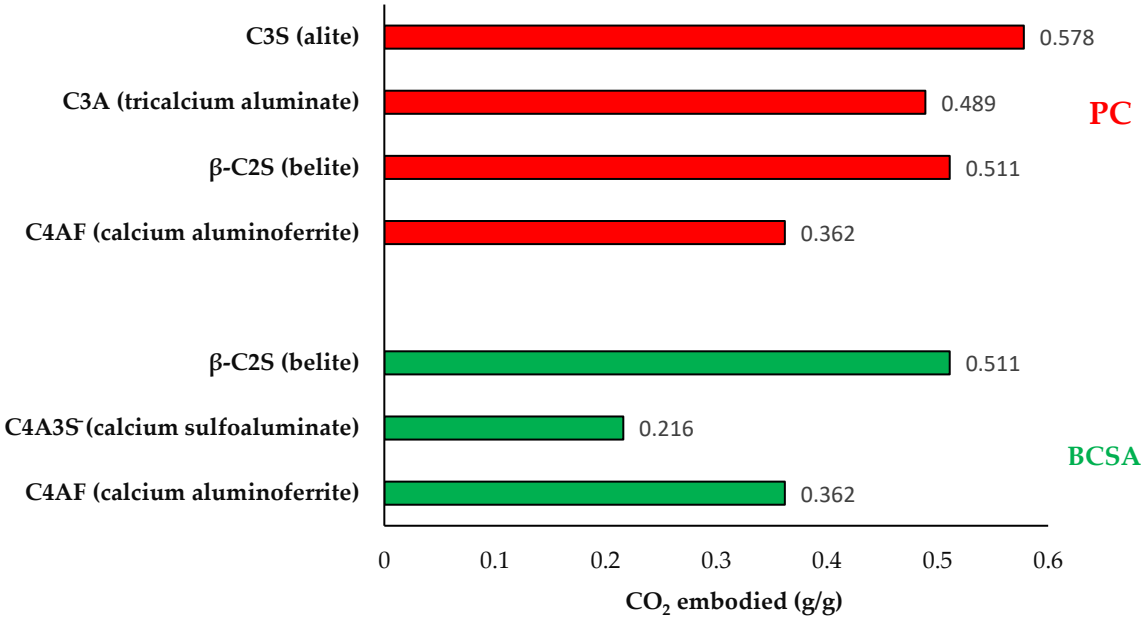

Figure 1. Embodied CO_2 in Portland and BCSA cement, by phase.

BCSA has been used for decades in the United States for accelerated airfield reconstruction [11], pavement repair [12], and structural rehabilitation [13]. These applications rely on the high early strength development of BCSA cement to accelerate construction and limit its impact on the end user. More recently, researchers have pondered the use of BCSA for structural applications. Specifically, the rapid-setting and sustainable characteristics of BCSA cement make it attractive for precast concrete construction. BCSA's rapid-setting

behavior accelerates release times and reduces reliance on energy-intensive steam-curing protocols. Furthermore, the reduced carbon footprint and embodied energy of BCSA cement would help the precast concrete industry achieve its sustainability goals and reduce its reliance on Portland cement.

While there is a large body of research on the material-scale performance and durability of BCSA cement concrete, there is very limited research on its performance in precast structural members. Research on the performance of precast BCSA concrete elements has been led by Ramseyer and Floyd at the University of Oklahoma, and later by Murray et al. at the University of Arkansas [14,15]. Murray at al. demonstrated construction of precast, prestressed BCSA concrete beams [15]. Successful construction of beams in as little as two hours from water addition to mold removal validated the feasibility of using BCSA cement to accelerate precast operations. Results showed that transfer and development lengths were in good agreement with AASHTO LRFD predictions, and load tests showed good agreement with predicted strengths, but prestress losses were far smaller than predicted.

Bowser studied the bond behavior of 0.6 in prestressing strands in eight 18-ft prestressed BCSA cement concrete beams and four prestressed Portland cement concrete (PCC) beams [16]. The researchers concluded that transfer lengths were approximately the same between BCSA and PCC beams; that ACI [17] and AASHTO [18] codes predicted transfer lengths in BCSA cement concrete reasonably well; that strands developed adequate bond relative to ACI 318 [17] requirements; and that prestress losses were significantly over-predicted for BCSA concrete beams.

The studies mentioned above are the only known articles that discuss the performance of prestressed BCSA concrete members. These papers have been of significant utility in demonstrating the feasibility of using BCSA cement concrete in a precast setting, and in validating (or invalidating) codified predictions of beam performance. However, the results of these studies must be validated for structural elements with widely varying composition and geometry before they can be generalized. Put simply: Much more data on the performance of full-scale BCSA cement concrete structural elements are needed before these materials can be adopted within concrete practice. To that end, this paper:

1. Demonstrates accelerated construction of a precast, prestressed voided deck slab bridge girder made with BCSA cement concrete;
2. Quantifies the performance of said girder in terms of material properties, transfer length, prestress losses, crack initiation and reopening, flexural strength, and shear strength; and
3. Compares measured performance with that predicted by with relevant ACI [17] and AASHTO [18] building codes.

2. Experimental Investigation

2.1. Materials

Concrete

Several trial mixes were conducted prior to reaching the final mix design with adequate setting time, workability, and compressive strength. Initially, the recommended ratios for cement, water, aggregates, and admixtures by the BCSA cement manufacturer were followed. The mix was modified by adjusting the ratios of the different materials to allow for the concrete to be mixed at the batch plant, delivered to the site, and placed in the forms without setting. Table 1 shows the final mix used to cast the full-scale specimens (details on full-scale specimens are given below). The final mix design reached the target compressive strength of 5000 psi in 4 h and had a final setting time of 1 h. Laboratory mixtures gave good workability, but the site-mixed concrete was too stiff to cast. A total of 200 lb (40 lb/yd^3) of water was added to the mixture to bring the mixture to a 6-in slump. The added water increased the water-to-cement ratio to 0.457, a 15.7% increase in water.

Table 1. BCSA concrete mix design.

BCSA Mixture Proportions		
BCSA	700	lb/cy
Water	280	lb/cy
Coarse aggregate	1650	lb/cy
Fine aggregate	1150	lb/cy
Air	6	%
Superplasticizer (GCP ADVA Cast 555)	98	fl oz/cy
Air entrainer (GCP Daravair 1000)	52.5	fl oz/cy
Retarder (GCP Recover)	182	fl oz/cy

Concrete was mixed in a twin-shaft high-speed mixer and charged into a drum truck for delivery to the prestressing bed. Full-scale specimens were cast, consolidated, and finished by plant personnel. Concrete cylinders (4 × 8 in), prisms (4 × 4 × 14 in), and other specimens were cast for measurements of setting time, mechanical properties, and shrinkage.

Early age measurements of setting time, autogenous shrinkage, and compressive strength were made at the precast plant, beginning immediately after casting. Setting time was measured by the mortar penetrometer method in accordance with ASTM C403 [19]. Compressive strength was measured in accordance with ASTM C39 [20] every 30 min following the measured final setting time. Autogenous shrinkage was measured by the corrugated tube method in accordance with ASTM C1698 [21].

Later-age measurements of mechanical properties and drying shrinkage were made after transportation of the specimens back to the laboratory. Compressive strength was measured in accordance with ASTM C39 [20]. Splitting tensile strength was measured in accordance with ASTM C496 [22]. Static modulus of elasticity was measured in accordance with ASTM C469 [23]. Dynamic modulus of elasticity, which is a nondestructive estimate of the modulus of elasticity of concrete based on the theory of wave propagation through solids, was measured in accordance with ASTM C215 [24]. Each of the preceding tests was performed on the date of full scale testing (concrete age of 110 days). Drying shrinkage was measured in accordance with the specifications of ASTM C157 [25] beginning at the final setting time and continuing until the specimens reached apparent equilibrium.

Table 2 lists the material properties of the concrete at the time of releasing the prestressing strands and on the day of full-scale testing. The results represent the average measured values of three specimens. The split tension tests showed high variability during the early age (first day); refer to Markosian for detailed material testing results [26].

Table 2. Concrete material properties.

	f'_c (psi)	f_{sp} (psi)	E	E_d (ksi)
Prestress release	4300	347	2200	3800
Full-scale testing	9760	-	2500	4000

2.2. Voided Deck Slab Bridge Girder

2.2.1. Casting

A precast, prestressed voided deck slab bridge girder was cast at a PCI-certified precast concrete plant. Figure 2 shows the geometry and detailed reinforcement of the beam. The beam was 22 ft long, 4 ft wide, and 21 in thick with three 10 in diameter polystyrene tubes used to create the voids as shown in Figure 2. The specimen was prestressed (pretensioned) using 22–0.6 in diameter Gr. 270 ksi low relaxation strands. The prestressing strands were detensioned by torching the strands (sudden release) once the required concrete release compressive strength was reached.

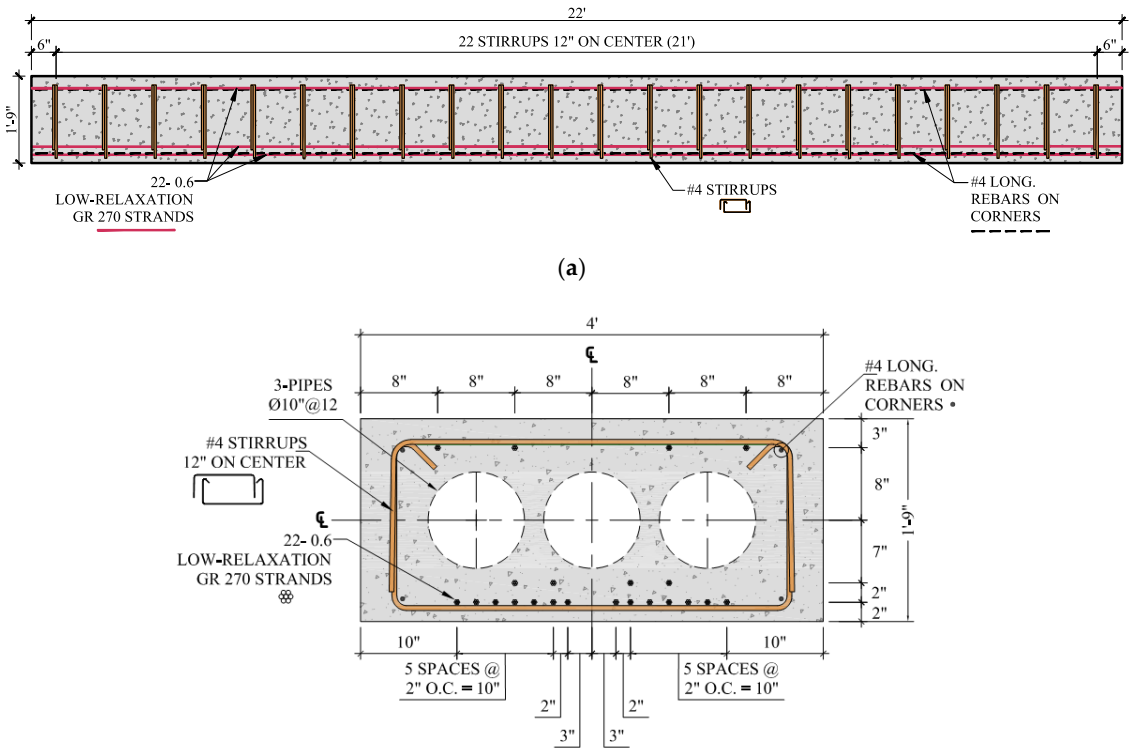

Figure 2. Full-scale specimen: (**a**) elevation and (**b**) cross section.

Detachable mechanical strain gages (DEMECs) were used at both ends of the specimen to measure the concrete surface strains at the level of prestressing strands to measure the transfer length. The DEMECs were placed at 2 in from the edge of the specimen and spaced at 4 in on center for 60 in. Prestressing losses were measured using vibrating wire strain gages (VWSGs) cast into the beam. A series of 8 total VWSGs were cast into the specimen and attached to the strands at both the top and bottom strands using zip ties, as shown in Figure 3. Four VWSGs were placed at mid-span: two on the top strands and two on the bottom. The remaining four gages were attached to top and bottom strands at quarter and three-quarter points along the length of the member. The VWSGs had both strain and temperature sensors, and readings were recorded once every 30 s for the lifetime of the beam before the final destructive tests. Camber was measured using an engineer's level and steel ruler accurate to one-tenth of a millimeter to calculate the change in elevation along the length of the member. Camber measurements were compared to the expected camber given in the AASHTO and PCI Bridge Design provisions. Both initial and long-term camber were measured [18,27].

Figure 3. Vibrating wire strain gage placement.

2.2.2. Testing

Figure 4 shows the midspan test setup along with the instrumentation plan used to test the full-scale prestressed voided bridge deck panel in flexure. The specimen was simply supported on pin and roller supports with a span length of 21-ft. A 400-kip load cell was concentrically placed under the 400-kip hydraulic ram, and two potentiometers were placed on each side of the deck at mid-span to measure the deflection during the test. Strand end slip was measured at both ends of the specimen using linear variable differential transformers (LVDTs) mounted to the strands, as shown in Figure 5. The LVDTs have a $+/-2$ in range and were calibrated to an accuracy of 0.0005 in. The crack initiation test consisted of a concentrated load centered over the bridge deck panel to induce cracking near the midspan of the specimen. The crack initiation test procedure consisted of incrementally increasing load and measuring the change in strain for each loading increment. Once a crack was initiated at midspan, the load was released and four strain transducers with 3 in gage length and accuracy of 1 $\mu\varepsilon$ were mounted across the initial crack for the crack reopening test using the same test setup used for the initial crack test. The crack reopening test was performed to evaluate the effective prestressing force in the specimen. The load was increased constantly until the crack reopened. After the crack reopening test was completed, the load was increased to failure to test the specimen for prestressing strand development length.

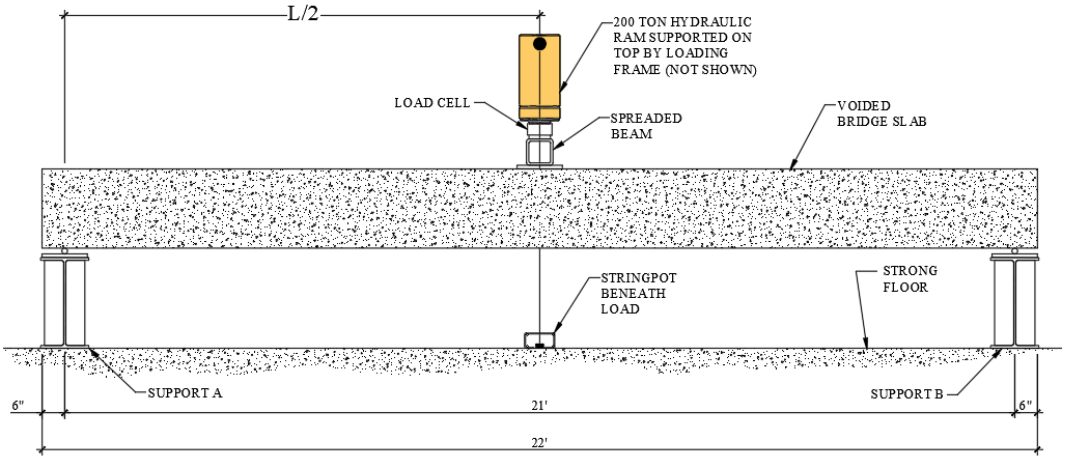

(**a**)

(**b**)

Figure 4. Midspan test setup and instrumentation: (**a**) test setup sketch and (**b**) test setup photo.

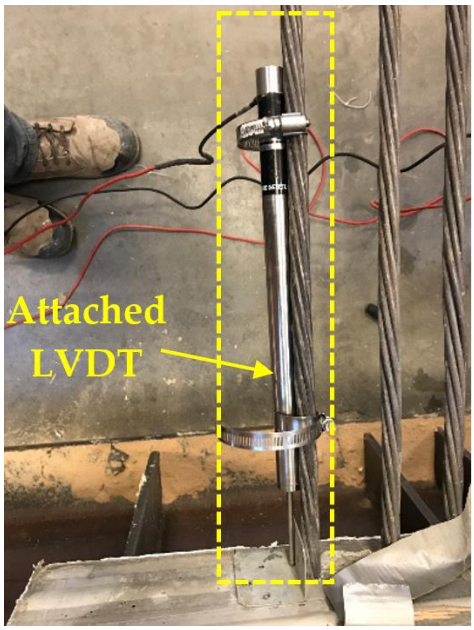

Figure 5. Strand end slip measurement using LVDT.

A test with the load placed at 1.25*d* from the face of the support, where *d* was the depth of the total section, was conducted after saw cutting the damaged half of the specimen during the midspan flexural test. Figure 6 shows the 1.25*d* test setup and instrumentation plan. The load was applied using two 400-kip hydraulic rams across the full width of the bridge deck using a spreader beam. Four LVDTs were mounted on the prestressing strands to measure the strand end slip. Wire potentiometers were placed on either side of the beam to measure the deflection at the applied load location.

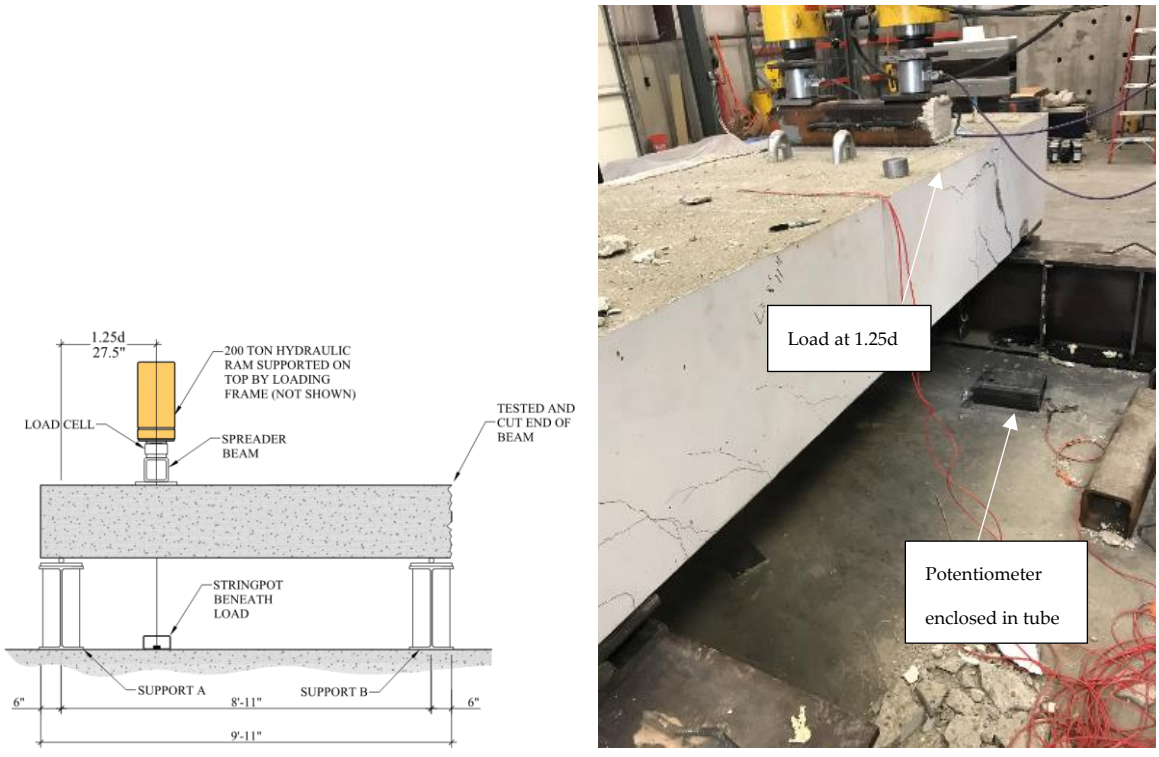

(**a**) (**b**)

Figure 6. 1.25*d* test setup and instrumentation: (**a**) test setup sketch, and (**b**) test setup photo.

3. Experimental Results

3.1. Transfer Length

The transfer length of the prestressing strands was measured at the live and dead ends of the specimen using DEMEC strain gauges and strand end slippage immediately after the prestressing release. Table 3 lists the measured and predicted transfer length values using AASHTO LRFD and ACI 318-14 [AASHTO, PCI, Markosian, ACI]. The measured values using DEMEC strain gauges used the least squares regression procedure along with the 95% average maximum strain (95% AMS) method to calculate the strain development profile. The transfer length was also calculated using strand end slippage using Guyon's formula (Equation (1)) [28]:

$$\ell_t = \alpha \frac{E_{ps}}{f_{ps}} \Delta_{es} \quad (1)$$

Table 3. Measured and predicted transfer length.

Beam End	Measured Transferred Length (in.)		Predicted Transfer Length (in.)	
	DEMEC	Strand end slip	AASHTO LRFD (60 L_d)	ACI 318-14 (50 L_d)
Live end	15.9	23	36	30
Dead end	15.9	22.9	36	30

The average measured transfer lengths using DEMEC and end slippage procedures were 15.90 and 22.95 in, respectively. The measured transfer lengths were significantly less than the predicted values of 36 and 30 in using AASHTO LRFD and ACI provisions, respectively. Measured transfer lengths at both ends using both methods yielded the same values. Calculated transfer length using the strand end slip method (Equation (1)) provided 44.6% longer transfer length than that of using DEMEC method. A similar trend was reported by Bowser [16]. However, measured transfer lengths using DEMEC and strand end slip methods are well below the predicted values by ACI 318-14 [17] and AASHTO LRFD [18].

3.2. Prestress Losses

3.2.1. Creep

The BCSA cement concrete creep was measured in accordance with ASTM C512 and compared to AASHTO predicted creep values, as shown in Figure 7a. AASHTO LRFD [18] predicted creep values were calculated at a constant time step to form the creep strain–time relationship using Equation (2). Measured humidity of 50% was used to calculate the predicted values.

$$\varepsilon_{CR} = \Delta f_{pCR} / E_{ps} \quad (2)$$

3.2.2. Shrinkage

Figure 7b shows measured and predicted shrinkage strain using AASHTO LRFD code provisions. Total shrinkage strain was calculated by combining autogenous and drying shrinkage. AASHTO LRFD provisions counts only for drying shrinkage using Eq. (3). The measured drying and autogenous shrinkage were conducted in accordance with ASTM C157 and ASTM C1698 standards, respectively.

$$\varepsilon_{SR} = \Delta f_{pSR} / E_{ps} \quad (3)$$

3.2.3. Total Prestressing Losses

Figure 8 shows the measured and predicted losses using AASHTO LRFD code provisions [18]. Predicted losses were computed using a relative humidity of 20% (measured by electronic psychrometer during casting). Measured losses were calculated using VWSG readings at midspan and quarter points along the length of the specimen. VWSG read-

ings were corrected for temperature using the manufacturer recommended procedures. Effective prestressing stress was computed using Equation (4):

$$f_{pe} = (\varepsilon_{pi} - \varepsilon) \times E_{ps} \quad (4)$$

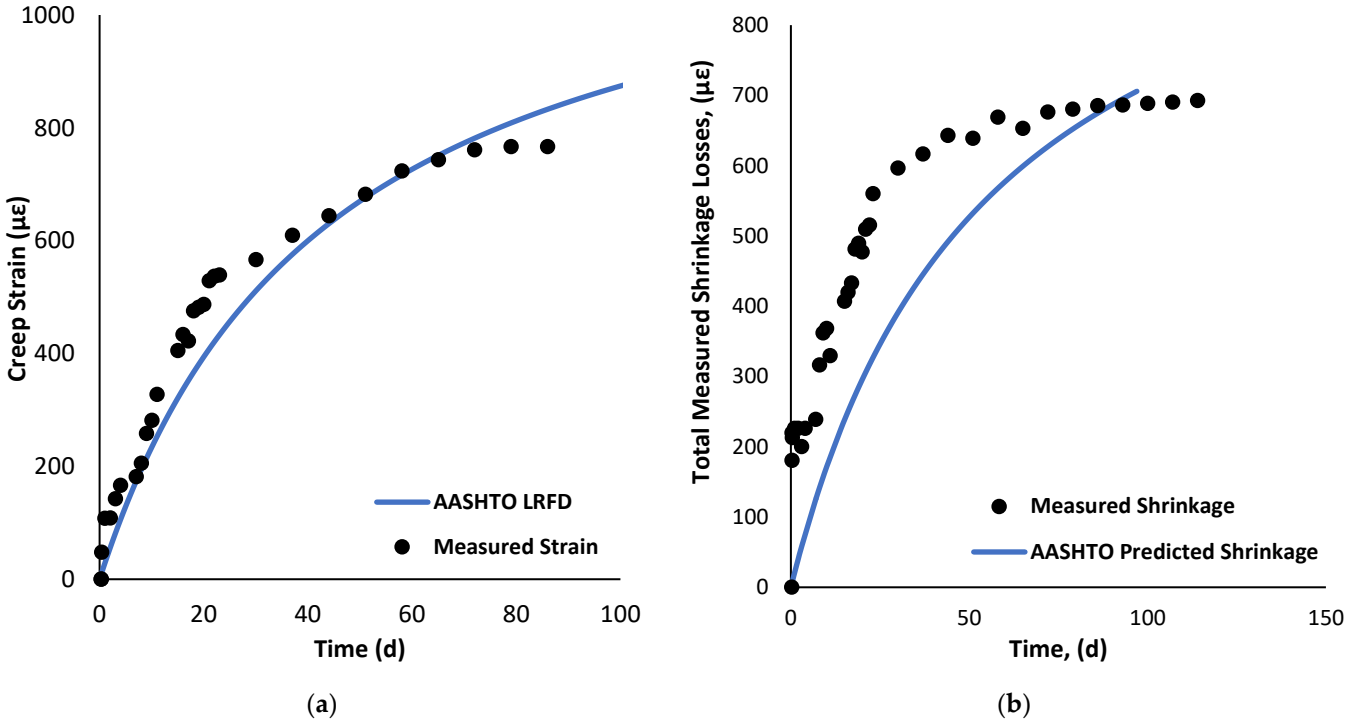

Figure 7. Measured vs. predicted: (**a**) creep strain; (**b**) shrinkage strain.

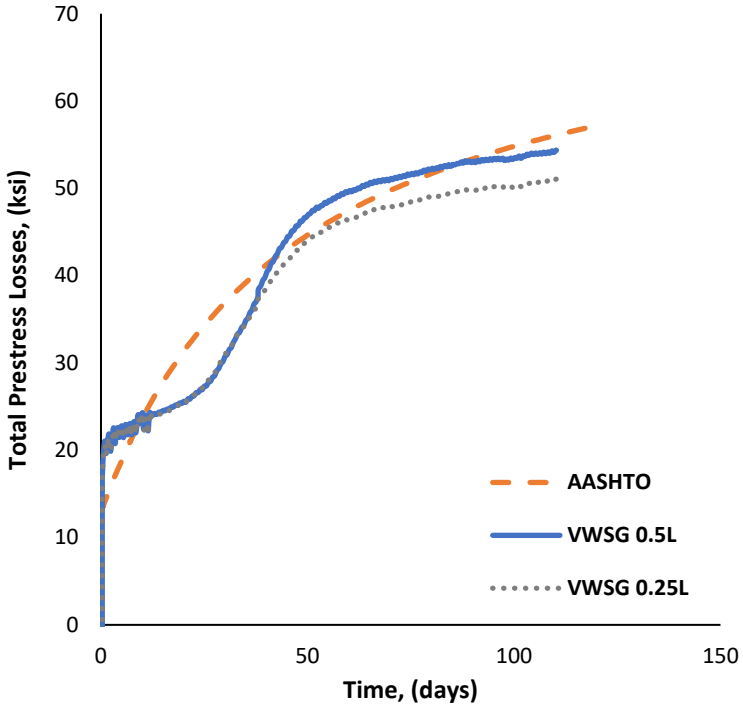

Figure 8. Average measured VWSG vs. predicted prestress losses.

3.2.4. Camber

Camber was measured immediately after transfer and over time until the time of testing. Measured camber after release was 0.28 in and at the time of testing was 1.26 in, which was 110 d after casting. The predicted initial and long-term camber using long-term PCI multipliers were 0.4 in and 0.972 in, respectively. The initial camber prediction was overestimated by 0.12 in and the long-term camber was underestimated by 0.288 in. This variation is not uncommon as the predicted values are approximate and the normal variations of the parameters used can cause ±20% deviation compared to predictions from Section 13.2.5 of the PCI Design Manual [27].

3.3. Beam Testing

3.3.1. Crack Initiation and Reopening

The load was applied monotonically at a constantly increasing rate until an initial crack was observed at midspan. Figure 9 shows the applied load–deflection relationship for the crack initiation test. The recorded load at the initiation of the first crack was 159.8 kips with a corresponding deflection of 0.008 in. Prestressing strand end slip was monitored during the crack initiation test and no end slippage was observed. After the observations of the crack initiation test were made, the load was released and the specimen was prepared for the crack reopening test. The applied load was increased until the load–deflection relationship experienced a nonlinear behavior and the initial crack was visible. Figure 10 shows the crack reopening load verses concrete strain across the crack. A least square regression analysis was performed on the load–strain relationship to identify the cracking load point at the intersection of the linear and nonlinear load–strain relationship. The measured crack reopening load was 83.12 kips with a strain reading of 190 $\mu\varepsilon$. The crack reopening load was used to estimate the effective prestressing stress in the beam using Equation (5):

$$f_{pe} = \frac{\frac{M_{tot} y_b}{I_n}}{\frac{A_p}{A_n} + \frac{A_p e_n y_b}{I_n}} \quad (5)$$

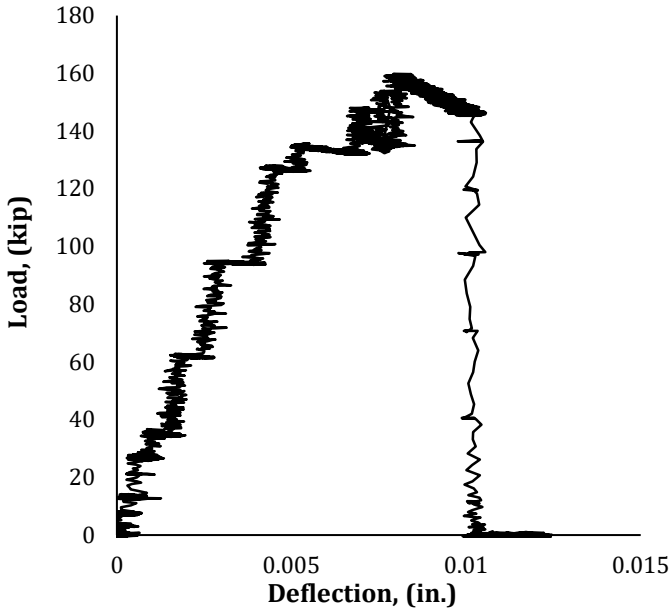

Figure 9. Load–deflection relationship for crack initiation test.

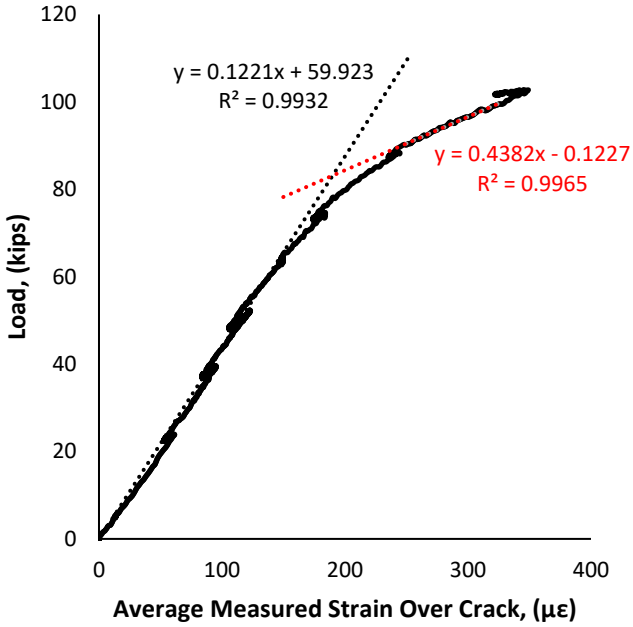

Figure 10. Crack reopening load–strain relationship.

The estimated effective prestressing stress was 138.2 ksi.

3.3.2. Load at Midspan

The crack reopening test was followed by an increased load until failure. Figure 11a shows the load–deflection relationship. Two distinct behaviors were observed, linear increase in deflection as the load resistance increased up to 160 kips, then non-linear deflection increase with lower rate of load resistance increase up to failure. Failure occurred at a maximum load of 258.6 kips, with a corresponding deflection of 2.1 in. The specimen failed suddenly in shear at mid-span following a diagonal crack at mid-span, as shown in Figure 11b. The failure was brittle as the load resistance suddenly dropped after the formation of the diagonal shear crack. Like the crack initiation test, the strand end slip was monitored throughout the test until failure and no strand end slippage was observed.

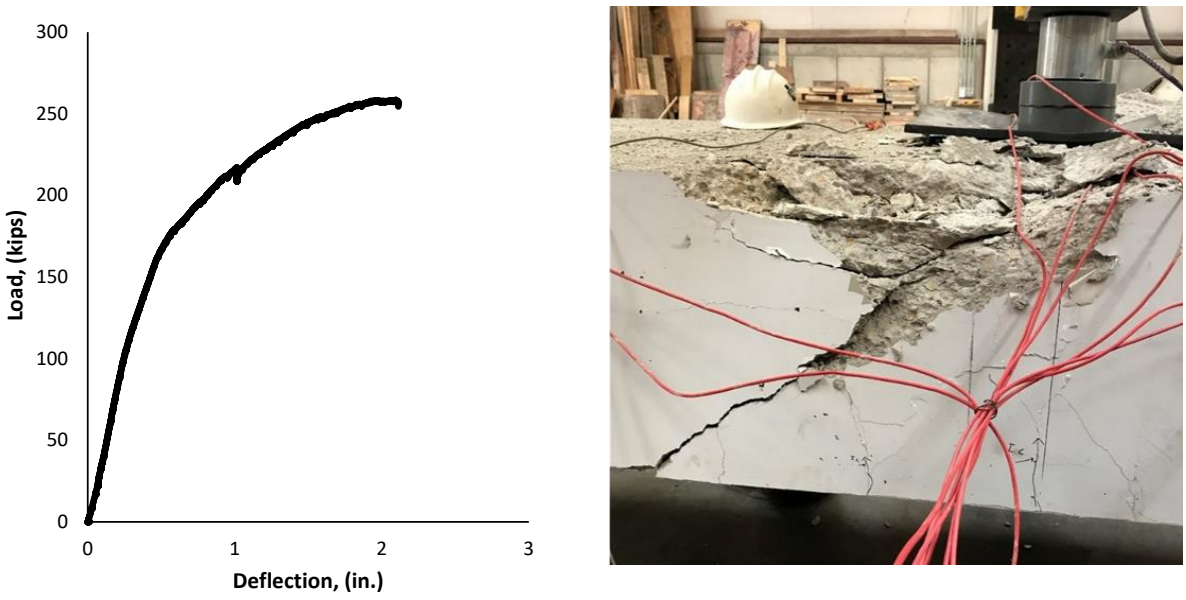

(**a**) (**b**)

Figure 11. (**a**) Load–deflection relationship and (**b**) failure mode when loaded at midspan.

3.3.3. Load at 1.25*d*

Figure 12a,b show the load-deflection and load-strand end slip relationships, respectively, for the 1.25*d* test. The specimen sustained a maximum applied load of 484.9 kips at a corresponding deflection of 0.194 in before significant strand slip. Flexural cracks directly under the load and shear-flexural cracks on the shear span were observed prior to failure, as shown in Figure 13. As the maximum load approached, the load resistance dropped as the strand slipped and flexural shear crack started to propagate parallel to the longitudinal axis of the member. The strand end slip was noticeable, as seen in Figure 12b, and audible during the test. The slipping of the strands corresponded to a loud metallic popping sound, followed by a noticeable jump in the slip at the time of the sound. Strand end slip corresponding to the maximum load of 484.9 kips was 0.0924 in. Final strand end slip was measured as 0.143 in after the load was released.

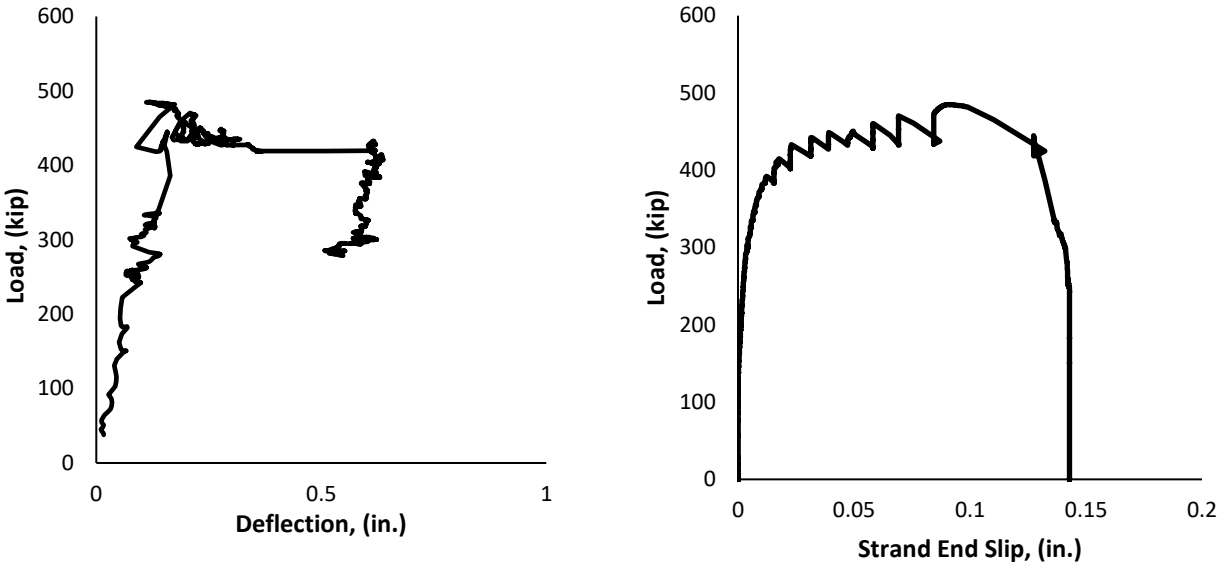

(**a**) (**b**)

Figure 12. (**a**) Load–deflection relationship and (**b**) load-strand end slip when loaded at 1.25*d*.

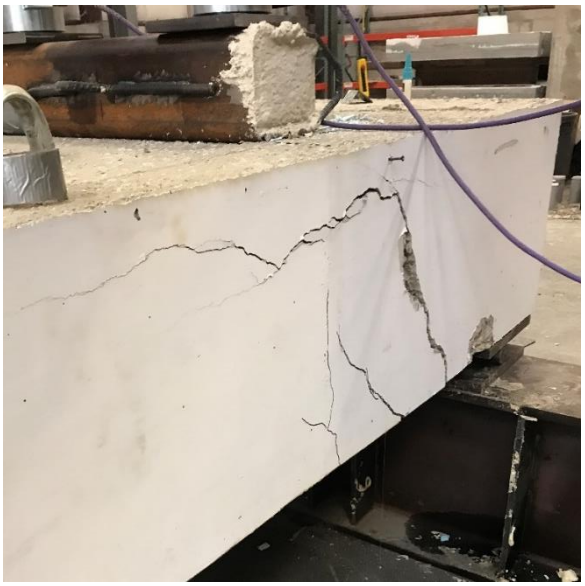

Figure 13. Failure mode when loaded at 1.25*d*.

4. Discussion

Measured creep strain for the BCSA cement was well predicted by AASHTO LRFD provisions, as shown in Figure 7. At an early loading age (first 60 days) predicted creep was nearly similar to the measured strains, however, after the first 60 days, the predicted creep strains values were overestimated.

The measured total shrinkage, which accounts for drying and autogenous shrinkage, was compared to predicted shrinkage values using AASHTO LRFD provisions. The predicted shrinkage strain values underestimated the measured values at an early age because AASHTO LRFD provisions considers drying shrinkage only and does not include autogenous shrinkage, which is significant in BCSA cement concrete. However, the long-term shrinkage strain was overestimated. The major reason for the underestimation in the early age of the concrete is that the autogenous shrinkage is measured without coarse aggregates. The coarse aggregates in concrete are not subject to shrinkage during curing as the paste in the concrete and it provides shrinkage restraint. Therefore, autogenous shrinkage strain, as measured using the standard test, is not necessarily accurate to include in the calculation of shrinkage losses. A more appropriate measure for this purpose would be to modify the autogenous shrinkage specimen such that it can accommodate large aggregate.

Prestress losses were measured using VWSGs cast into the concrete, material testing, and crack reopening test and the measured effective prestressing stress were 145.7, 149.5, and 138.2 ksi, respectively. Effective prestress for BCSA cement concrete was higher than the AASHTO predicted value (139.1 ksi) for all measured values of effective prestress except that of the crack reopening test. The average measured effective prestress for BCSA cement concrete was 144.5 ksi +/− 5.8 ksi. If the average measured effective prestress is taken as the actual effective prestress, then AASHTO predicts effective prestress for BCSA cement concrete with reasonable accuracy for the period investigated. Based on the material testing, it is likely that the AASHTO equations to estimate prestress losses will overestimate long-term losses. Further investigation is warranted.

The moment capacity of the specimen was calculated using moment curvature analysis, using Response 2000 software, and strain compatibility procedures [29]. The measured moment strength due to the applied point load at mid-span was 1290 kip-ft, while the predicted capacity using moment curvature analysis and strain compatibility were 1466.2 and 1458.4 kip-ft, respectively. Figure 14 shows the moment–curvature relationship calculated at mid-span. The specimen did not achieve the predicted nominal flexural strength due to shear failure at mid-span. The predicted shear strength using the modified compression field theory (MCFT) per AASHTO LRFD shear design provisions was 116.8 kips, while the applied shear at failure was 129.3 kips. Full bridge analysis showed that the ultimate moment at mid-span was associated with a corresponding ultimate shear of 25 kips, which is much lower than the applied shear force (129.3 kips), due to the concentrated point load at mid-span. Therefore, the observed shear failure mode will not occur in real bridge loading configuration.

Moment capacity at $1.25d$ was calculated using AASHTO LRFD provisions for flexural strength and using the bond-slip model. The bond-slip model developed in Figure 15 compares the AASHTO development length model to the measured development and transfer length. The AASHTO model shows a rapid stress increase in the prestressing strands from the end of the beam to the transfer length, with a slower gain in stress along the development length. The measured stress in the strands was found by performing a strain compatibility analysis using the power stress–strain formula [30] for calculating stress in the strands (f_{ps}). The value of f_{ps} given in the bond model represents the maximum stress in the strands at any location along the beam. A bond-slip failure occurs when the stress in the strands exceeds the maximum stress as given in the bond model. The measured stress in the strands due to the maximum applied load of 484.9 kips at the applied load location was calculated as 257 ksi. However, the AASHTO model predicted the maximum stress in the strands as 104.35 ksi. The extrapolated development length was calculated by

extending the measured stress–strain curve at the same slope until reaching a maximum stress of 270 ksi. Additionally, the measured shear strength at 1.25*d* was compared to the predicted value using AASHTO LRFD MCFT procedures. The measured shear strength was 367 kips, while the predicted nominal shear strength was 227 kips. The demand for a bridge using the full-length girder only requires an ultimate shear at the critical section of 133 kips, which is significantly lower than the applied shear of 367 kips. Measured shear resistance was significantly higher than the predicted and required shear strength, which is not unusual for deck panel bridge type when testing close to the disturbed region [31].

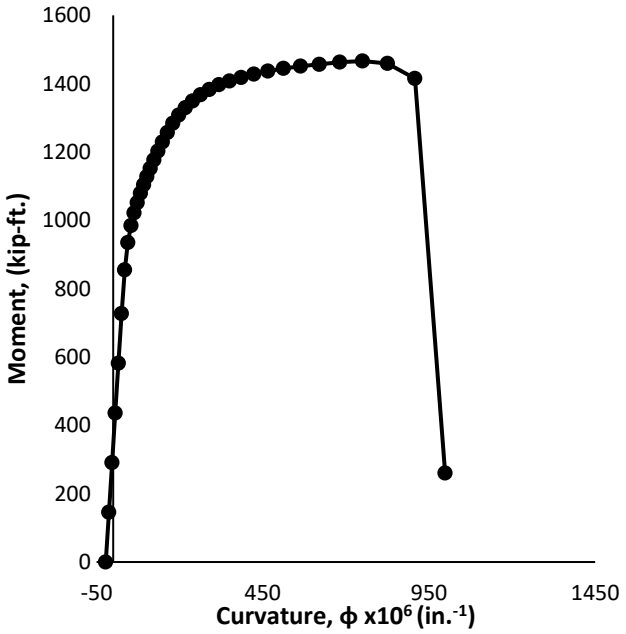

Figure 14. Moment–curvature relationship obtained from Response 2000.

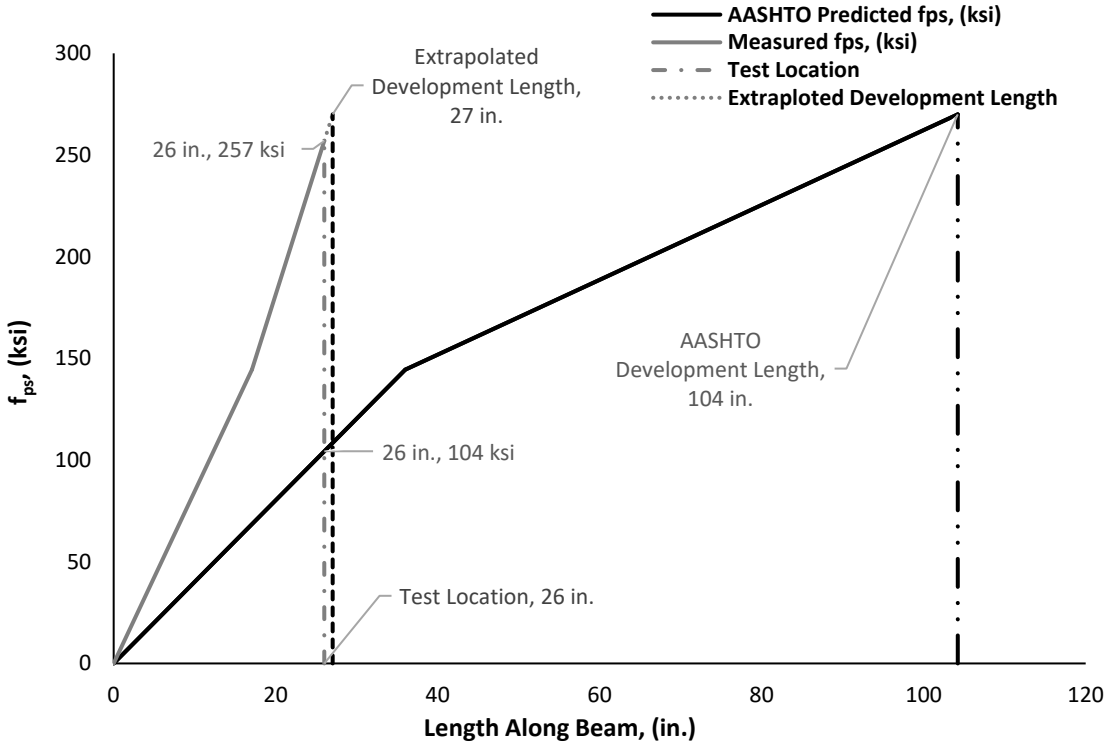

Figure 15. Prestressing strand bond model.

5. Summary and Conclusions

A precast, prestressed voided deck slab bridge girder mimicking a full-scale in-service bridge in Utah was cast using BCSA cement concrete. The full-scale specimen was tested in a variety of configurations, and the resulting performance was compared with the predictions from relevant design codes. The results of the study demonstrate the feasibility of using BCSA cement concrete—a sustainable alternative to traditional Portland cement concrete—in precast, prestressed concrete construction. However, the results also suggest that existing building codes do not always accurately predict the beam performance. Specifically, the results of this study suggest:

- Creep and shrinkage strains were generally well predicted using AASHTO for BCSA cement concrete during the period of monitoring, but if trends continued, likely would overestimate both shrinkage and creep. Based on these results AASHTO predictions for losses are likely accurate enough for design and will be conservative for long-term predictions.
- Autogenous shrinkage for BCSA cement is significantly larger than in Portland cement, therefore it is important to include this behavior when estimating losses, though this is not currently explicitly covered in AASHTO LRFD provisions.
- The average measured effective prestress for BCSA cement concrete was 144.5 ksi $+/-$ 5.8 ksi and showed good agreement with the AASHTO LRFD-predicted effective prestress for the time period predicted indicating safe use of AASHTO LRFD effective prestress provisions for BCSA concrete.
- The maximum applied shear for the mid-span test was 129.0 kips, while the AASHTO predicted nominal shear strength was 116.8 kips which is commensurate with the observed shear failure. Bridge loading analysis indicated shear envelope design is only 25 kips, which is much lower than the applied shear force (129.3 kips), due to the concentrated point load. Therefore, the observed failure mode will not occur in real bridge loading configuration and was only observed because of the testing conditions. These results indicate prediction of shear capacity for BCSA concrete members is accurate and conservative for the situation tested.
- No strand-end slip was observed during the mid-span testing indicating strands were fully developed for the applied moment of 1290 kip-ft with a development length of 11 ft.
- During the 1.25d test, the specimen failed at 484.9 kips after considerable strand slip, indicating bond failure. The calculated strand stress (f_{ps}) at failure was 256.9 ksi, which significantly exceeded the predicted value of 104.35 ksi using AASHTO LRFD transfer and development lengths criteria.
- Using the measured transfer length and the strand stress results from the 1.25d bond failure test, the expected embedment length to achieve 270 ksi in the strand is 27 in, much shorter than the 104 in predicted by the AASHTO LRFD bond length model. This indicates the use of AASHTO LRFD can be conservative in predicting the transfer and development length for BCSA concrete for the strength and strands used in this study.

Author Contributions: Conceptualization, M.M. (Marc Maguire) and R.J.T.; methodology, M.M. (Marc Maguire) and R.J.T.; formal analysis, N.M., R.T.; investigation, N.M. and M.M. (Marc Maguire); writing—original draft preparation, N.M. and R.T.; writing—review and editing, all; visualization, N.M., R.T., M.M. (Mohammad Mastali); supervision, M.M. (Marc Maguire) and R.J.T.; project administration, M.M. (Marc Maguire); funding acquisition, M.M. (Marc Maguire) and R.J.T. All authors have read and agreed to the published version of the manuscript.

Funding: This paper is based on research supported by the Mountain Plains Consortium Project Number 560. Any observations, findings, recommendations, or conclusions presented in this publication are those of the authors and do not necessarily reflect the views of the Mountain Plains Consortium. The APC was funded by the University of Nebraska-Lincoln.

Institutional Review Board Statement: Not applicable.

Informed Consent Statement: Not applicable.

Data Availability Statement: The data presented in this study are available in the article.

Acknowledgments: The authors are grateful to Olympus Precast for their donation of the full-scale bridge member and use of their facilities.

Conflicts of Interest: The authors declare no conflict of interest. The funders had no role in the design of the study; in the collection, analyses, or interpretation of data; in the writing of the manuscript, or in the decision to publish the results.

Nomenclature

A_n	transformed area of cross section
A_p	area of prestressing strands
d	total depth of concrete section
E_c	static modulus of elasticity of concrete
E_d	dynamic modulus of elasticity of concrete
e_n	eccentricity of prestressing strands about center of gravity of cross section
E_{ps}	static modulus of elasticity of prestressing strand
f_{pe}	effective prestressing stress
f_{ps}	stress in prestressing strand just prior to transfer
f_{sp}	splitting tensile strength of concrete
I_n	transformed moment of inertia of cross section
ℓ_t	transfer length
M_{tot}	total applied moment including self-weight
y_b	distance from bottom concrete tension fiber to center of gravity of cross section
α	shape factor of the bond stress distribution constant ($\alpha = 2$ *or* 3 for constant or linear stress distribution, respectively). Constant stress distribution was assumed in this study.
Δ_{ps}	prestressing strand end slip
ε	measured strain in prestressing strand
ε_{pi}	initial strain in prestressing strand
ε_{CR}	predicted creep strain
Δf_{pCR}	prestress loss due to creep calculated using AASHTO LRFD Eq. 5.9.5.4.2b-1
Δf_{pSR}	prestress loss due to shrinkage calculated using AASHTO LRFD Eq. 5.9.5.4.2a-1

References

1. Klein, A. Calcium Aluminosulfate and Expansive Cements Containing Same. U.S. Patent 3,155,526, 3 November 1964.
2. Mehta, P.K.; Klein, A. Investigations on the Hydration Products in System 4CaO-3Al2O3-SO3-CaSO4-CaO-H2O. In *Highway Research Board Special Report*; Highway Research Board: Washington, DC, USA, 1966; pp. 328–352.
3. Ost, B.W.A.; Schiefelbein, B.; Summerfield, J.M. Very High Early Strength Cement. U.S. Patent 3,860,433, 14 January 1975.
4. Thomas, R.; Maguire, M.; Sorensen, A.; Quezada, I. Calcium Sulfoaluminate Cement. *Concr. Int.* **2018**, *40*, 65–69.
5. Habert, G. Assessing the environmental impact of conventional and 'green' cement production. In *Eco-efficient Construction and Building Materials*; Pacheco-Torgal, F., Cabeza, L.F., Labrincha, J., de Magalhães, A., Eds.; Woodhead Publishing: Sawston, UK, 2014; pp. 199–238.
6. Glasser, F.P.; Zhang, L. High-performance cement matrices based on calcium sulfoaluminate-belite compositions. *Cem. Concr. Res.* **2001**, *21*, 1881–1886. [CrossRef]
7. Ambroise, J.; Péra, J. Immobilization of calcium sulfate contained in demolition waste. *J. Hazard. Mater.* **2008**, *151*, 840–846. [CrossRef] [PubMed]
8. Jewell, R.B. Influence of Calcium Sulfoaluminate Cement on the Pullout Performance of Reinforcing Fibers: An Evaluation of the Micro-Mechanical Behavior. Ph.D. Thesis, Civil Engineering, University of Kentucky, Lexington, KY, USA, 2015.
9. Gartner, E. Industrially interesting approaches to "low-CO2" cements. *Cem. Concr. Res.* **2004**, *34*, 1489–1498. [CrossRef]
10. Gartner, E.; Sui, T. Alternative cement clinkers. *Cem. Concr. Res.* **2018**, *114*, 27–39. [CrossRef]
11. Bescher, E.; Stremfel, J.; Ramseyer, C. The Role of Calcium Sulfoaluminate in Concrete Sustainability. In Proceedings of the Twelfth International Conference on Recent Advances in Concrete Technology and Sustainability Issues, Prague, Czech Republic, 1 October 2012.
12. Bescher, E.; Kim, J. Belitic Calcium Sulfoaluminate Cement: History, Chemistry, Performance, and Use in the United States. In Proceedings of the 1st International Conference on Innovation in Low Carbon Cement and Concrete Technology, London, UK, 25 June 2019.

13. Maggenti, R.; Gomez, S.; Luena, R. Bridge Hinge Reconstruction. *Struct. Mag.* **2015**, 30–32. Available online: https://www.structuremag.org/wp-content/uploads/2014/12/F-BridgeHinge-Maggenti-Jan151.pdf (accessed on 14 July 2021).
14. Floyd, R.W.; Ramseyer, C. Behavior of Precast, Prestressed Calcium Sulfoaluminate Cement Concrete Beams. In Proceedings of the PCI Convention and National Bridge Conference, Nashville, TN, USA, 5 March 2016.
15. Murray, C.D.; Floyd, R.W.; Ramseyer, C.C.E. Using belitic calcium sulfoaluminate cement for precast, prestressed concrete beams. *PCI J.* **2019**, *64*, 55–67. [CrossRef]
16. Bowser, T. Development Length of 0.6 in. In *Prestressing Strands in Precast, Prestressed Calcium Sulfoaluminate Cement Concrete, M.S. in Civil Engineering*; University of Oklahoma: Norman, OK, USA, 16 December 2016.
17. ACI Committee 318. *Building Code Requirements for Structural Concrete (ACI 318-14) and Commentary (ACI 318R-14). Farmington Hills*; American Concrete Institute: Michigan, MI, USA, 2014.
18. American Association of State Highway and Transportation Officials (AASHTO). In *LRFD Bridge Design Specifications*, 7th ed.; AASHTO: Washington, DC, USA, 2014.
19. ASTM C403/C403M-16. *Standard Test Method for Time of Setting of Concrete Mixtures by Penetration Resistance*; ASTM International: West Conshohocken, PA, USA, 2016.
20. ASTM C39/C39M-18. *Standard Test Method for Compressive Strength of Cylindrical Concrete Specimens*; ASTM International: West Conshohocken, PA, USA, 2018.
21. ASTM C1698-14. *Standard Test Method for Autogenous Strain of Cement Paste and Mortar*; ASTM International: West Conshohocken, PA, USA, 2014.
22. ASTM C496/496M-17. *Standard Test Method for Splitting Tensile Strength of Cylindrical Concrete Specimens*; ASTM International: West Conshohocken, PA, USA, 2017.
23. ASTM C469/C469M-14e1. *Standard Test Method for Static Modulus of Elasticity and Poisson's Ratio of Concrete in Compression*; ASTM International: West Conshohocken, PA, USA, 2014.
24. ASTM C215-19. *Standard Test Method for Fundamental Transverse, Longitudinal, and Torsional Resonant Frequencies of Concrete Specimens*; ASTM International: West Conshohocken, PA, USA, 2019.
25. ASTM C157/C157M-17. *Standard Test Method for Length Change of Hardened Hydraulic-Cement Mortar and Concrete*; ASTM International: West Conshohocken, PA, USA, 2017.
26. Markosian, N. Calcium Sulfoaluminate Cement Concrete for Prestressed Bridge Girders: Prestressing Losses, Bond, and Strength Behavior. Master's Thesis, Utah State University, Logan, UT, USA, 2019.
27. *PCI Bridge Design Manual*, 3rd ed.; Precast/Prestressed Concrete Institute: Chicago, IL, USA, 2014.
28. Guyon, Y. *Prestressed Concrete*; John Wiley & Sons: New York, NY, USA, 1960.
29. Bentz, E.C. Sectional Analysis of Reinforced Concrete Members. Ph.D. Thesis, University of Toronto, Toronto, ON, Canada, 2000.
30. Tawadrous, R.; Morcous, G. Shear Strength of Deep Hollow-Core Slabs. *ACI Struct. J.* **2018**, *115*, 699–709. [CrossRef]
31. Devalapura, R.K.; Tadros, M.K. Stress-Strain Modeling of 270 ksi Low-Relaxation Prestressing Strands. *PCI J.* **1992**, *32*, 100–106. [CrossRef]